Supporting Information for "Multichannel singular spectrum analysis of InSAR datasets: data-adaptive interpolation and decomposition of Sentinel-1 time series at Pacaya Volcano, Guatemala"

D. Walwer[1], J. Gonzalez-Santana[1], C. Wauthier[1,2], E. Calais[3,4]& M. Ghil[3,5,6]

[1]Department of Geosciences, The Pennsylvania State University, University Park, PA, USA

[2]Institute for Computational and Data Sciences, The Pennsylvania State University, University Park, PA, USA

[3]Département de Géosciences, École normale supérieure, Université PSL; Paris, France

[4]Université Côte d'Azur, Institut de Recherche pour le Développement, CS, Observatoire de la Côte d'Azur, Géoazur; Valbonne, France.

[5]Department of Atmospheric & Oceanic Sciences, University of California at Los Angeles, Los Angeles, CA, USA

[6]Department of Mathematics, Imperial College London, London, UK

Contents of this file

1. Text S1. InSAR data processing
2. Text S2. SVD approach to M-SSA
3. Text S3. Computing the reconstructed components $r_{lk}(t)$ of length N
4. Text S4. Alternative criteria for selecting M-SSA gap filling optimal parameters
5. Text S5. Applying M-SSA to large datasets
6. Text S6. Applying M-SSA to large datasets using the SVD approach

7. Text S7. M-SSA analysis applied simultaneously to vertical and East–West components

8. Text S8. M-SSA analysis of LOS time series from descending and ascending acquisitions

9. Figure S1. LOS datasets from ascending and descending acquisitions

10. Figure S2. Comparing gap filling estimates using various values of M

11. Figure S3. Comparing gap filling estimates with a priori removed data points

12. Figure S4. Spatial and frequency distributions of gap-filling optimal parameters

13. Figures S5-S6. Results of applying M-SSA analysis simultaneously on vertical and East–West displacements

14. Figures S7-S9. M-SSA analysis results for LOS time series from descending and ascending acquisitions

Text S1. InSAR data processing

Here we briefly review information presented by Gonzalez-Santana and Wauthier (2021) concerning InSAR Sentinel-1 data processing and refer the reader to that article and the references therein for further information.

The vertical and East–West InSAR displacements obtained for Pacaya and presented in the main text are produced by combining InSAR line-of-sight (LOS) displacement time series from ascending and descending acquisitions. These LOS time-series are presented in Figure S1 and analyzed in Section S6. They were produced using the Small BAselines Subset (SBAS) method (Berardino et al., 2002) which relies on selecting pairs of images with small perpendicular (perpendicular distance between the satellite positions) and temporal (time between acquisitions) baselines in order to minimize geometric and

temporal decorrelation, respectively. This strategy allows to make use of SAR products despite difficulties associated to the tropical regions of Central America (Ebmeier et al., 2013).

SAR pairs were processed using GAMMA (Werner et al., 2000). Topographic contributions were removed using a 12 m TanDEM-X digital elevation model. The interferograms were smoothed with an adaptive spectral filter (Goldstein & Werner, 1998). Unwrapping of the InSAR phase was performed with a Minimum Cost Flow algorithm on a triangular irregular network.

Small Baseline Subset (SBAS) time series analysis was performed individually on Sentinel-1 ascending and descending acquisitions and two sets of LOS displacements time series were therefore obtained for Pacaya using Sentinel-1 (Figure S1).

To produce the vertical and East–West InSAR displacement presented and exploited in the main text (Figure 2), we made use of the Multidimensional SBAS (MSBAS) (Samsonov & d'Oreye, 2012). MSBAS was applied to the ascending and descending Sentinel-1 datasets that are overlapping from 2014 to 2020.

Text S2. Computing the reconstructed components (RCs) of length N

The time series in $\mathbf{R}_k$ presented in the main text have length N'. One can produce filtered versions of the time series $x_l(t)$ of length N corresponding to the k^{th} EOF using

$$r_{lk}(n) = \frac{1}{M_n} \sum_{j=L_n}^{U_n} A_k(n-j+1) E_l^k(j). \tag{1}$$

The normalization factor and the summation bounds differs between the central part of the time series and their ends and are given by:

$$(M_n, U_n, L_n) = \begin{cases} (n, 1, n), & 1 \le n \le M-1, \\ (M, 1, M), & M \le n \le N', \\ (N'-n+1, n-N+M, M), & N'+1 \le n \le N; \end{cases} \tag{2}$$

see Ghil and Vautard (1991) and Ghil et al. (2002) for details.

Text S3. Alternative criteria for selecting M-SSA gap filling optimal parameters

The scheme described in the main text to select the optimal pair of parameters (M_0, k_0) relies on minimizing the NRMSE between the variance of the original time series with the missing points and the estimated one that includes the values $r_{k\ell}(t^*)$.

Alternatively, and following (Kondrashov et al., 2005), one can also minimize the NRMSE between randomly removed data points and their estimates produce with the M-SSA gap filling algorithm. This NRMSE, is computed only at the epochs at which values were originally available. Using the optimal parameter pair (M_0, k_0) produces, therefore, time series that are as close as possible to the original time series at the points at which the values were originally known. This approach provides readily similar results as the ones presented in the main text. However, the values of optimal parameters (M_0, k_0) obtained this way change each time data points are randomly selected to be removed from the time series.

Text S4. Applying M-SSA to large datasets

Here we provide algebraic details regarding the method of applying M-SSA to large datasets proposed by Groth, Feliks, Kondrashov, and Ghil (2016). Following their approach, we start by noticing that the S-PCs expression $\mathbf{y} = \mathbf{xe}$ can be translated into

$$\mathbf{Y} = \mathbf{X}\left(\mathbf{e} \otimes \mathbf{I}_M\right), \tag{3}$$

where $\mathbf{I}_M$ is an identity matrix of size M and $\otimes$ denotes the Kronecker product. Multiplying both sides of (3) by their respective transposes,

$$\mathbf{Y}^{\mathrm{t}}\mathbf{Y} = (\mathbf{e} \otimes \mathbf{I}_M)^{\mathrm{t}}\, \mathbf{X}^{\mathrm{t}}\mathbf{X}\, (\mathbf{e} \otimes \mathbf{I}_M)\,, \tag{4}$$

and substituting the covariance matrices $\mathbf{Y}^{\mathrm{t}}\mathbf{Y}$ and $\mathbf{X}^{\mathrm{t}}\mathbf{X}$ by their eigendecomposition $\mathbf{V}^{\mathrm{t}}\mathbf{\Lambda}\mathbf{V}$ and $\mathbf{E}^{\mathrm{t}}\mathbf{\Sigma}\mathbf{E}$, respectively, yields

$$\mathbf{V}^{\mathrm{t}}\mathbf{\Lambda}\mathbf{V} = (\mathbf{e} \otimes \mathbf{I}_M)^{\mathrm{t}}\, \mathbf{E}^{\mathrm{t}}\mathbf{\Sigma}\mathbf{E}\, (\mathbf{e} \otimes \mathbf{I}_M)\,. \tag{5}$$

The matrix $(\mathbf{e} \otimes \mathbf{I}_M)$ is orthogonal and so is $\mathbf{E}\,(\mathbf{e} \otimes \mathbf{I}_M)$. It follows that $\mathbf{X}$ and $\mathbf{Y}$ have the same eigenvalues, $\mathbf{\Lambda} = \mathbf{\Sigma}$, and also that:

$$\mathbf{E} = (\mathbf{e} \otimes \mathbf{I}_M)\, \mathbf{V}\mathbf{T}, \tag{6}$$

with $\mathbf{T}$ a diagonal matrix of elements $\{1, -1\}$. Equation (6) means that the eigenvectors of $\mathbf{X}^{\mathrm{t}}\mathbf{X}$ are, up to a sign, determined by the eigenvectors of $\mathbf{Y}^{\mathrm{t}}\mathbf{Y}$.

The EOFs derived from $\mathbf{Y}$ can then be used to express the RCs $\mathbf{R}_k$ of $\mathbf{X}$ using equation (7) of the main text and equation (6) here:

$$\mathbf{R}_k = \mathbf{X}\,(\mathbf{e} \otimes \mathbf{I}_M)\, \mathbf{V}^{\mathrm{t}}\mathbf{K}\mathbf{V}^{\mathrm{t}}\left(\mathbf{e}^{\mathrm{t}} \otimes \mathbf{I}_M\right) = \mathbf{V}\mathbf{K}\mathbf{V}^{\mathrm{t}}\left(\mathbf{e}^{\mathrm{t}} \otimes \mathbf{I}_M\right). \tag{7}$$

The filtered versions of $\mathbf{Y}$ represent $\mathbf{R}^{(Y)} = \mathbf{Y}\mathbf{V}\mathbf{K}\mathbf{V}^{\mathbf{t}}$ so that:

$$\mathbf{R}_k = \mathbf{R}^{(Y)}\left(\mathbf{e}^{\mathrm{t}} \otimes \mathbf{I}_M\right). \tag{8}$$

Upon channel-wise averaging along skew diagonals on either side of (8) we finally obtain the relation

$$\mathbf{r}_k = \mathbf{r}_k^{(Y)}\mathbf{e}^{\mathrm{t}} \tag{9}$$

presented in the main text and relating the RCs of $\mathbf{y}$ with the RCs of $\mathbf{x}$.

Text S5. Singular value decomposition (SVD) approach to M-SSA

The eigenvectors constituting the empirical basis of functions presented in the main text and obtained through the eigendecomposition of either $\mathbf{C}^{(V)}$ or $\mathbf{C}^{(P)}$ can also be obtained through the SVD of the matrix $\mathbf{X}$:

$$\mathbf{X} = \eta \mathbf{P} \mathbf{\Lambda}^{\mathbf{1/2}} \mathbf{V}^{\mathrm{t}}. \tag{10}$$

Here $\mathbf{\Lambda}$ is diagonal and $\eta = \max\{D \times M, N - M + 1\}$ is the convenient normalization. The vectors contained in $\mathbf{P}$ and $\mathbf{V}$ are the eigenvectors of $\mathbf{C}^{(\mathbf{P})}$ and $\mathbf{C}^{(\mathbf{V})}$ respectively and the non-zeros diagonal elements of $\mathbf{\Lambda}$ are either the nonzero eigenvalues $\lambda_k^{(P)}$ or $\lambda_k^{(V)}$ provided by the eigendecomposition of $\mathbf{C}^{(\mathbf{P})}$ and $\mathbf{C}^{(\mathbf{V})}$.

Text S6. Applying M-SSA to large datasets using the SVD approach

Here we review in somewhat greater detail the approach of Groth et al. (2016) for large data sets using the SVD approach to M-SSA. The SVD of $\mathbf{Y} = \mathbf{USW}'$ and $\mathbf{X} = \mathbf{P}\Lambda\mathbf{V}'$ substituted into (3) yield

$$\eta^{1/2} \mathbf{USW}^{\mathrm{t}} = \eta^{1/2} \mathbf{P} \Lambda \mathbf{V}^{\mathrm{t}} \left(\mathbf{e} \otimes \mathbf{I}_M \right). \tag{11}$$

Since the SVD of a real-valued matrix is unique up to a pairwise change in the sign of the singular vectors, it follows that $\mathbf{X}$ and $\mathbf{Y}$ have the same singular values, and that

$$\mathbf{P} = \mathbf{UT}, \tag{12a}$$

$$\mathbf{V} = \left(\mathbf{e} \otimes \mathbf{I}_M \right) \mathbf{WT}, \tag{12b}$$

with $\mathbf{T}$ a diagonal matrix whose elements are $\{1, -1\}$. It follows that the left and right singular vector of $\mathbf{X}$ are, therefore, up to their sign, determined by the singular vectors of $\mathbf{Y}$ and by $\mathbf{e}$. It follows that the same operations presented above in Section S2 can be applyied to express $\mathbf{r}_k$ as a function of $\mathbf{r}^{(Y)}$.

Text S7. M-SSA analysis applied simultaneously to vertical and East–West components

In the main text, we presented M-SSA analysis applied to InSAR vertical and horizontal displacements separately. Here we briefly present the result of M-SSA analysis performed on both components simultaneously. While analyzing separately the two components is useful to highlight their differences, analyzing the two of them together allows one to compare more directly the spatio-temporal modes of variability they share.

The results are presented in Figures S5 and S6. The dominant frequencies of the main modes extracted this way are consistent with the ones presented in the main text. The pairs of oscillatory modes have dominant frequencies at 1, 2, 3, 4, 5.8 and 6.8 cy/yr, like the ones extracted either from the vertical or the East–West displacements alone (Figure S6).

Two nonlinear trends are extracted: one capturing mainly the long-periodic trend of the vertical displacement (PC#3) and the other one capturing a long-periodic signal in the East–West component (PC#5) (Figure S6). Both of them have a dominant frequency around 0.3cy/yr.

The spatial patterns associated with each of the above mentioned modes are displayed in Figure S6 for both components. They are all consistent with the ones presented in the main text in Figures 7 and 8.

Text S8. M-SSA analysis of LOS time series from descending and ascending acquisitions

We also performed our M-SSA analysis directly on the line-of-sight (LOS) time series used to produce the vertical and East–West displacement time series used in the main

text. Because the LOS time series have fewer data points than the vertical and East–West components time series, the M-SSA gap filling algorithm did not work well on the former. To produce evenly sampled time series for LOS data, we used a simpler approach and filled the gaps using the following model

$$x_\ell(t^*) = a + b + \sigma r, \tag{13}$$

where $x_l(t^*)$ is an estimate of the missing data, a and b are the slope and intercept of the regression line, respectively, r is a Gaussian random variable with zero mean and unit standard deviation, while σ is the standard deviation of the original detrended time series x_ℓ. Filling gaps in this way is justified by the fact that Gaussian noise is not correlated in time or space and is thus going to be seen by M-SSA as part of the noise, rather than of the trends or oscillatory signals (Walwer et al., 2016, and references therein).

The results of applying M-SSA analysis on LOS time series are displayed in Figures S7–S9. The main pairs of oscillatory modes have dominant frequencies at 1, 2, 3, 5.8 and roughly 7cy/yr, which is consistent with the results presented in the main text; see Figure S7. Nonlinear trends with dominant frequencies at about 0.3cy/yr are extracted from both ascending and descending datasets as well. The nonlinear trends extracted from LOS data in the descending acquisition show the same spatial patterns as the ones extracted from the vertical displacement: higher amplitude at high elevation and within the 2014 lava flow.

References

Berardino, P., Fornaro, G., Lanari, R., & Sansosti, E. (2002). A new algorithm for surface deformation monitoring based on small baseline differential sar interferograms. *IEEE Transactions on geoscience and remote sensing*, *40*(11), 2375–2383.

Ebmeier, S. K., Biggs, J., Mather, T. A., & Amelung, F. (2013). Applicability of insar to tropical volcanoes: insights from central america. *Geological Society, London, Special Publications*, *380*(1), 15–37.

Ghil, M., Allen, M. R., Dettinger, M. D., Ide, K., Kondrashov, D., Mann, M. E., ... others (2002). Advanced spectral methods for climatic time series. *Reviews of Geophysics*, *40*(1), 3–1. Retrieved 2014-12-08, from `http://onlinelibrary.wiley.com/doi/10.1029/2000RG000092/full`

Ghil, M., & Vautard, R. (1991). Interdecadal oscillations and the warming trend in global temperature time series. *Nature*, *350*, 324–327.

Goldstein, R. M., & Werner, C. L. (1998). Radar interferogram filtering for geophysical applications. *Geophysical research letters*, *25*(21), 4035–4038.

Gonzalez-Santana, J., & Wauthier, C. (2021). Unraveling long-term volcano flank instability at Pacaya Volcano, Guatemala, using satellite geodesy. *Journal of Volcanology and Geothermal Research*, *410*, 107147. Retrieved 2021-11-04, from `https://linkinghub.elsevier.com/retrieve/pii/S0377027320305837` doi: 10.1016/j.jvolgeores.2020.107147

Groth, A., Feliks, Y., Kondrashov, D., & Ghil, M. (2016). Interannual variability in the North Atlantic ocean's temperature field and its association with the wind stress forcing. *Journal of Climate*, *30*. (published online) doi: 10.1175/jcli-d-16-0370.1

Kondrashov, D., Feliks, Y., & Ghil, M. (2005). Oscillatory modes of extended Nile River records (A.D. 622–1922). *Geophysical Research Letters*, *32*(10), L10702. Retrieved 2015-03-03, from http://onlinelibrary.wiley.com/doi/10.1029/2004GL022156/abstract doi: 10.1029/2004GL022156

Samsonov, S., & d'Oreye, N. (2012). Multidimensional time-series analysis of ground deformation from multiple InSAR data sets applied to Virunga Volcanic Province. *Geophysical Journal International*, *191*(3), 1095–1108.

Walwer, D., Calais, E., & Ghil, M. (2016, March). Data-adaptive detection of transient deformation in geodetic networks: DATA-ADAPTIVE GPS TIME SERIES ANALYSIS. *Journal of Geophysical Research: Solid Earth*, *121*(3), 2129–2152. Retrieved 2016-05-11, from http://doi.wiley.com/10.1002/2015JB012424 doi: 10.1002/2015JB012424

Werner, C., Wegmüller, U., Strozzi, T., & Wiesmann, A. (2000). Gamma sar and interferometric processing software. In *Proceedings of the ers-envisat symposium, gothenburg, sweden* (Vol. 1620, p. 1620).

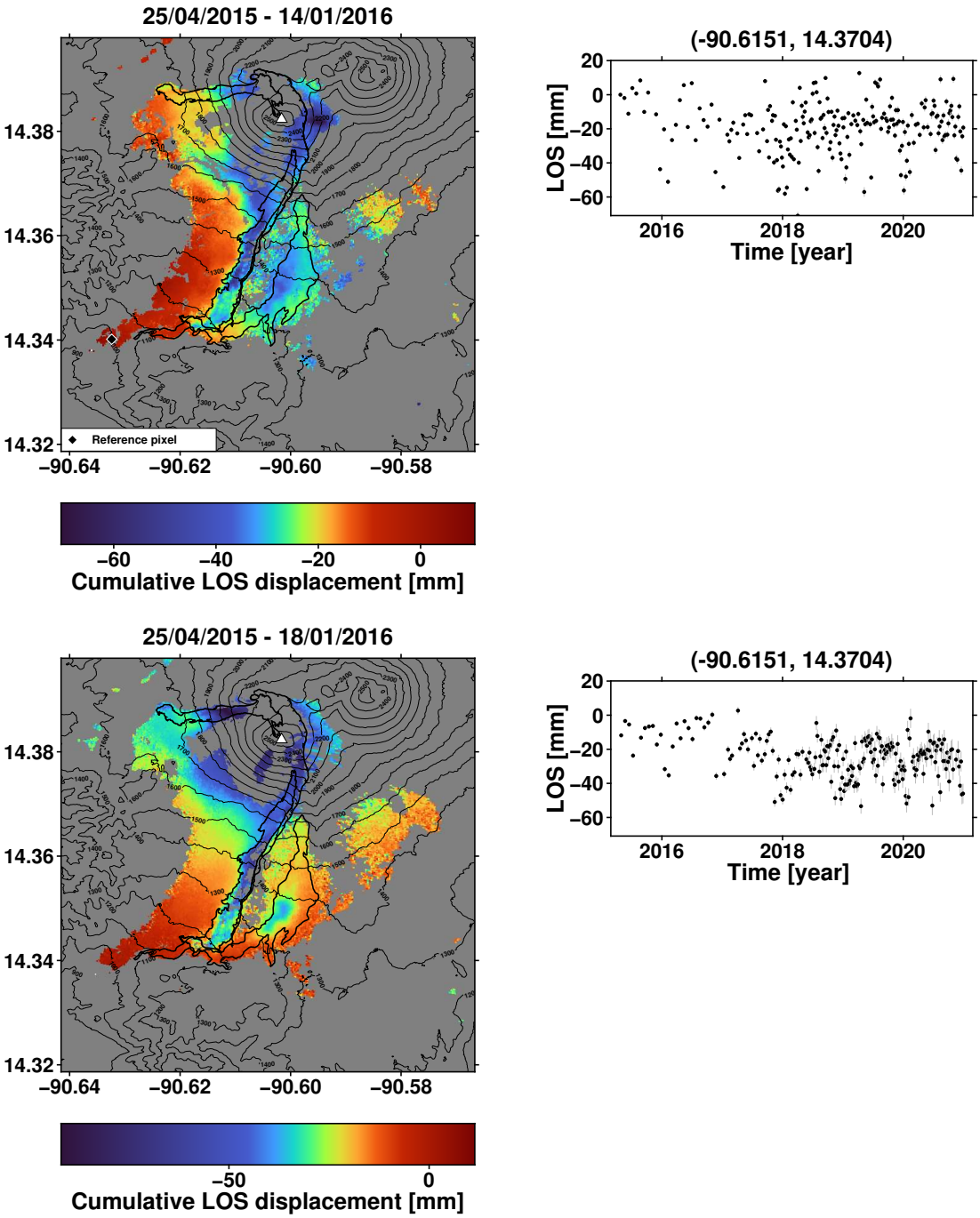

Figure S1. Sentinel-1 dataset for Pacaya volcano. a) Examples of two InSAR scenes showing cumulative LOS from ascending acquisitions (top) and descending acquisitions (bottom). b) Examples of InSAR time series from ascending and descending acquisitions.

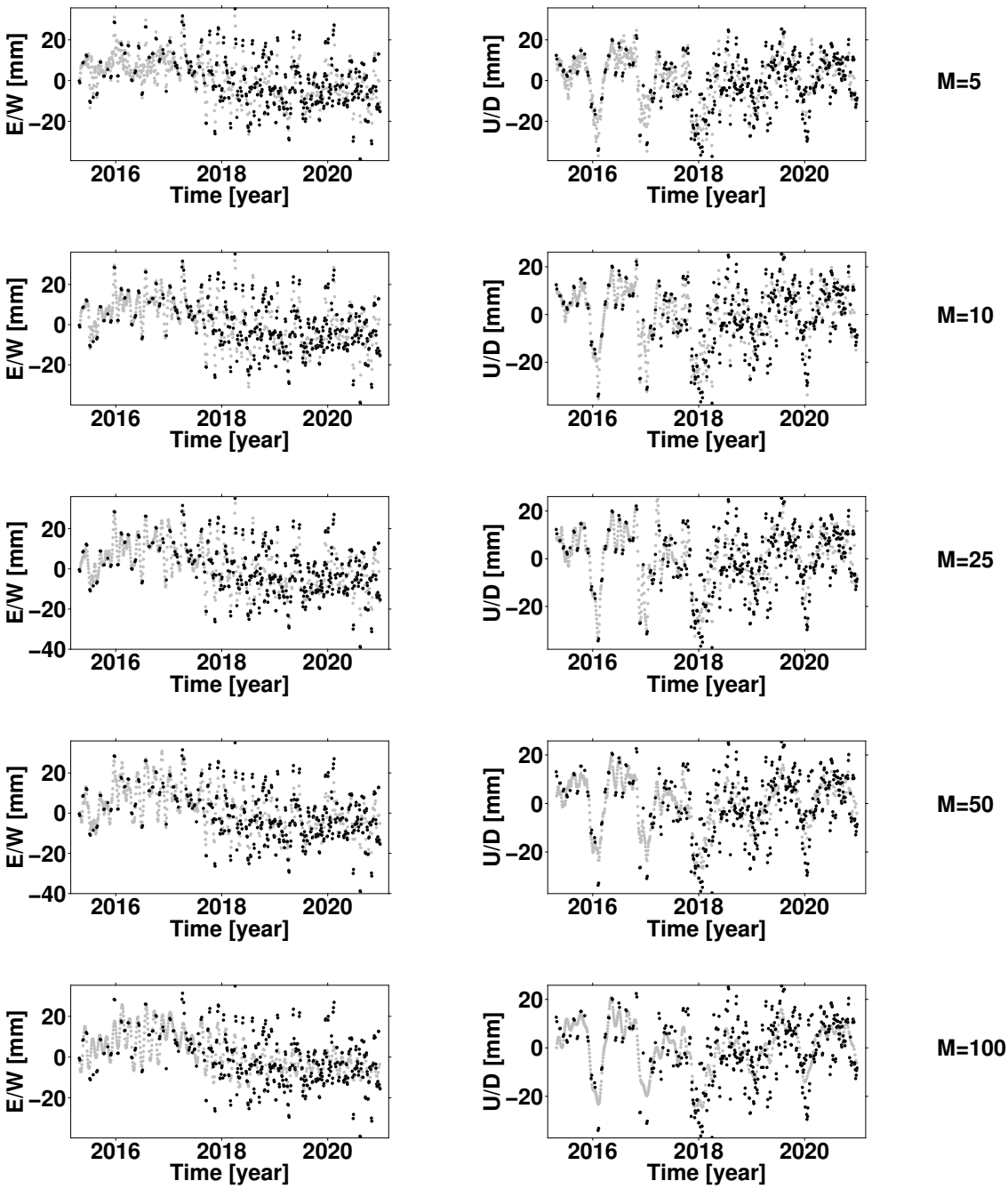

Figure S2. Comparison between results from the M-SSA gap filling algorithm using different values of M and $k = 10$ for time series located at pixel coordinates (-90.6120, 14.3684). Original (black dots) and final (grey dots) time series. Grey dots correspond to the data points obtained with the M-SSA gap filling algorithm. The final uniform-sampling interval is $\tau_s = 2$ days.

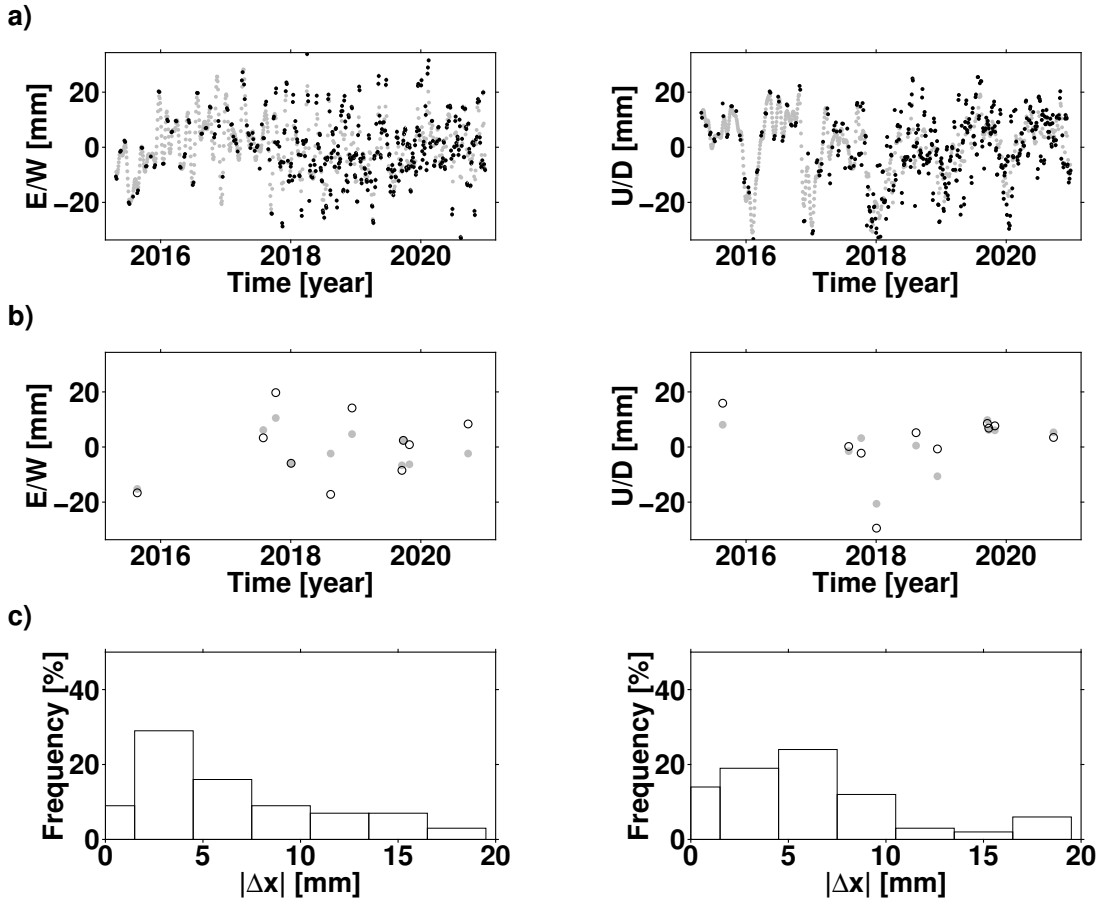

Figure S3. Comparing values of randomly removed data points with estimated values from the M-SSA gap filling algorithm. a) Original (black dots) and interpolated values (grey dots) time series. The final uniform-sampling interval is $\tau_s = 2$ days. b) Comparison between values of randomly removed data points (open black circles) and corresponding estimated values (grey filled circles). c) Frequency distribution of the absolute value of the difference between randomly removed data points and the corresponding estimates $|\Delta x|$ for a group of horizontal displacement time series (Left) and vertical displacement time series (Right).

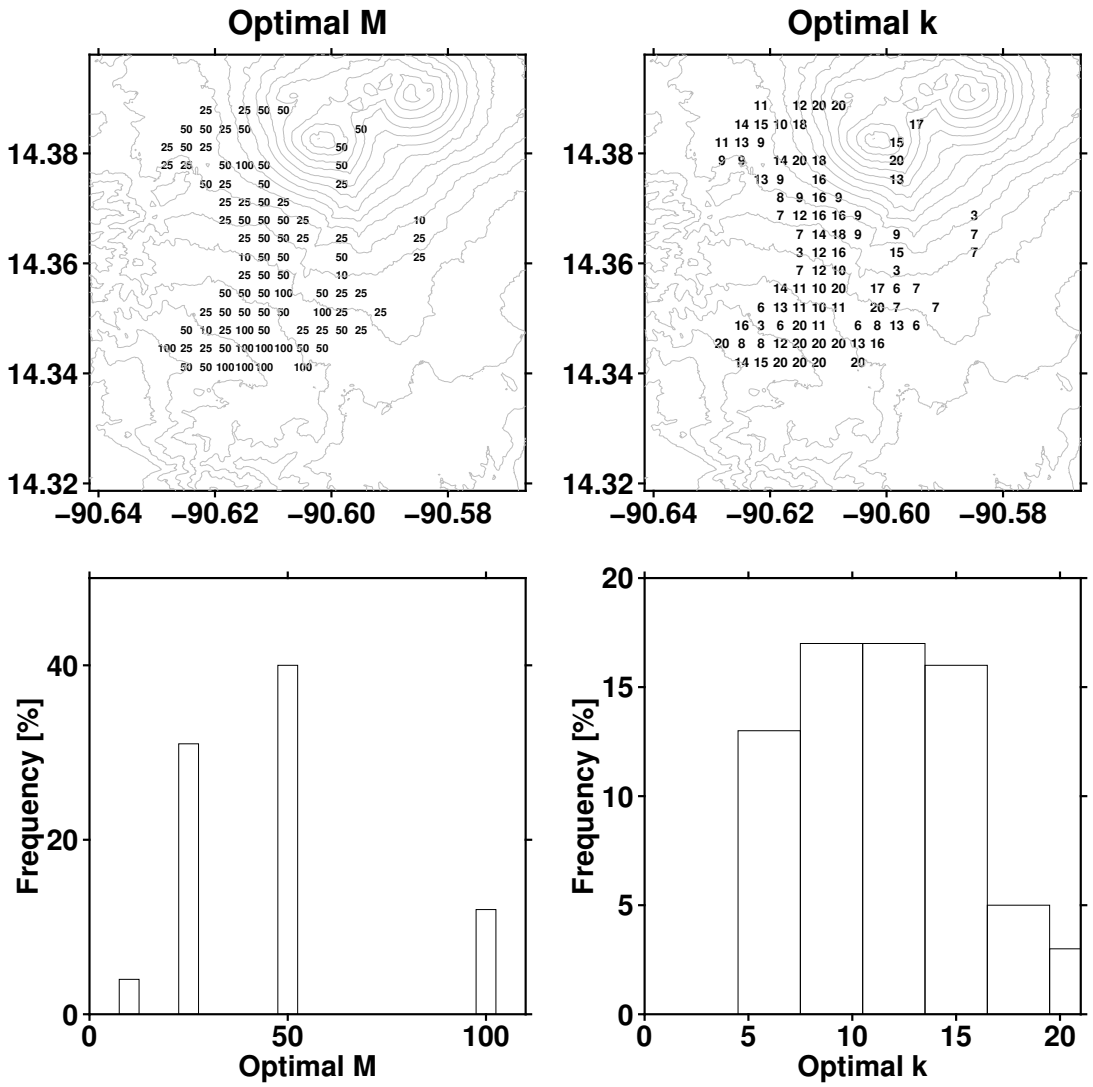

Figure S4. Distributions of optimal parameter values for the gap filling algorithm presented in the main text. Top: Maps showing the spatial distribution of optimal parameters M at selected pixels locations (Left) and spatial distribution of optimal number of modes k used for the corresponding optimal M (Right). Bottom: Histogram showing the frequency distributions of optimal parameter values M and k.

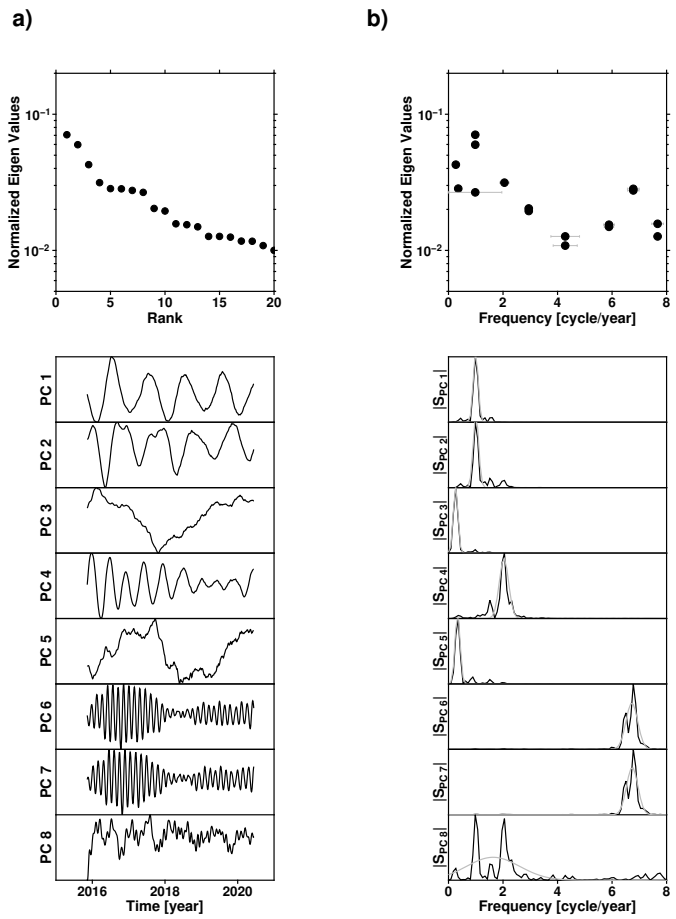

Figure S5. M-SSA decompositions of InSAR vertical and East/Displacement analyzed simultaneously. a) Normalized eigenvalues sorted in decreasing order of variance captured. Lower panels show the first 8 PCs. Note that oscillatory modes are characterized by pairs of nearly equal eigenvalues with their corresponding PCs in phase quadrature see for example PC1 and PC2. b) Spectral-domain representation of the M-SSA decomposition. Upper panels display the normalized eigenvalues obtained using equation sorted according to the dominant frequency of the associated PC. Lower panels show the power spectra of the 8 leading PCs and the associated Gaussian fit in frequency f (horizontal gray line).

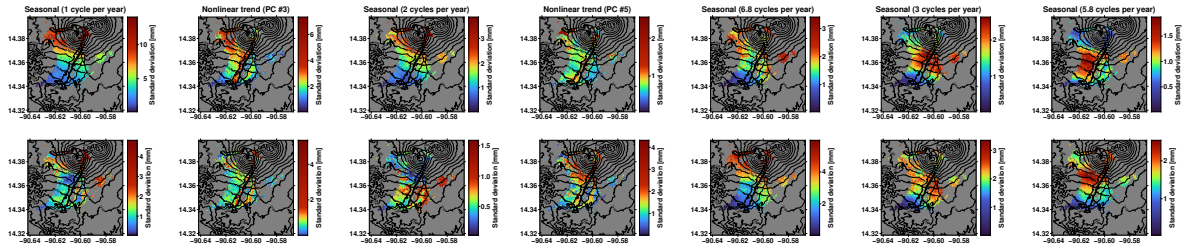

Figure S6. Spatial patterns of the amplitude of the dominant seasonal oscillations and trends extracted from the M-SSA analysis performed on vertical and East–West displacements simultaneously.

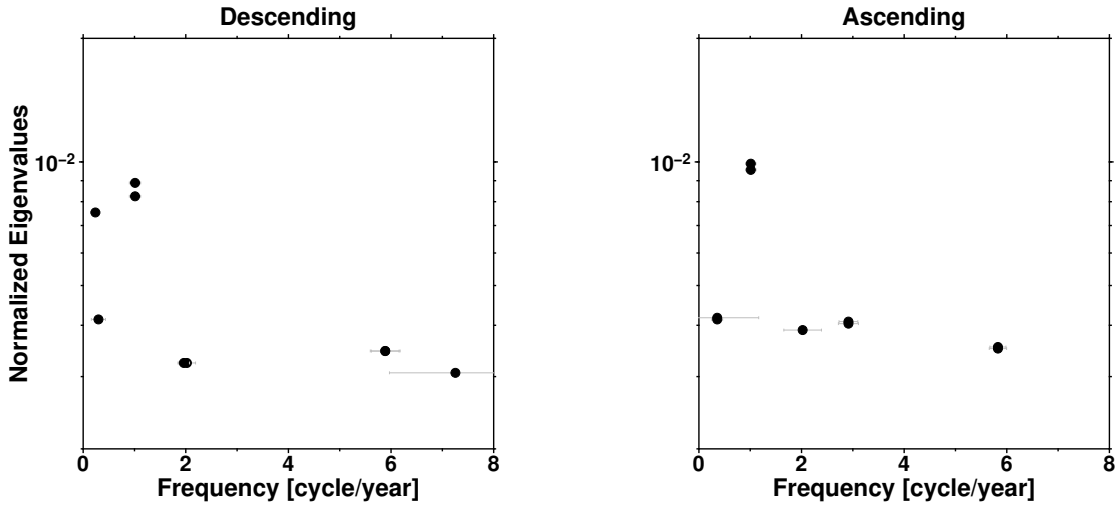

Figure S7. Normalized eigenvalues sorted according to the dominant frequency of the associated PC and extracted from M-SSA decomposition of LOS datasets from descending (Left) and ascending (Right) acquisitions.

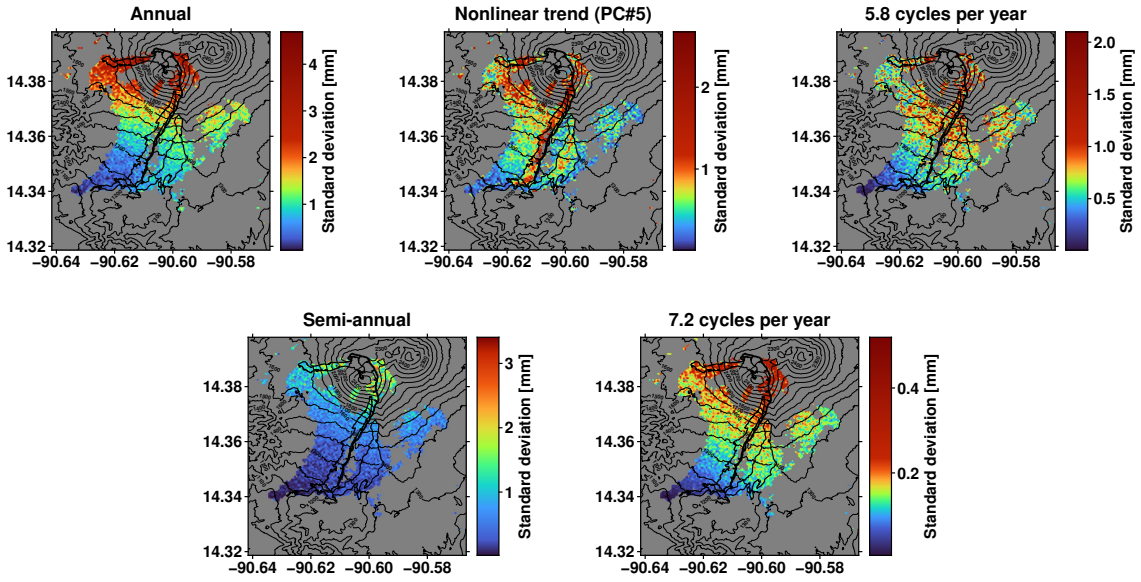

Figure S8. Spatial patterns of the amplitude of the dominant seasonal oscillations and trend extracted from M-SSA analysis on LOS datasets at Pacaya.

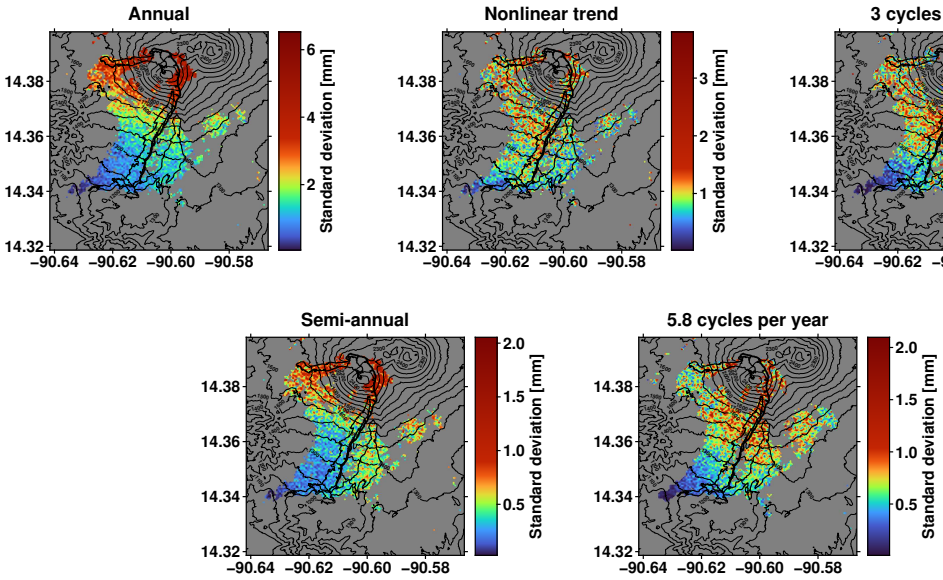

Figure S9. Spatial patterns of the amplitude of the dominant seasonal oscillations and nonlinear trend extracted from the M-SSA analysis applied to LOS datasets at Pacaya.